Materials Today Bio 29 (2024) 101285

Contents lists available at ScienceDirect

Materials Today Bio

journal homepage: www.journals.elsevier.com/materials-today-bio

One arrow two eagles: Multifunctional nano-system for macrophage reprogramming and osteoclastogenesis inhibition against inflammatory osteolysis

Tong Sha [a,c,1], Ze Wang [b,1], Jinwei Li [a,c], Yahong Wu [a,c], Jinbiao Qiang [a,c], Zhenming Yang [a,c], Yue Hu [d], Kaijuan Zheng [a,c], Shuyu Zhang [a,c], Haizhu Sun [e], Andrew K. Whittaker [f], Bai Yang [b], Hongchen Sun [a,c], Quan Lin [b,**], Ce Shi [a,c,*]

[a] Department of Oral Pathology, Hospital of Stomatology, Jilin University, Changchun, 130021, PR China
[b] State Key Laboratory of Supramolecular Structure and Materials, College of Chemistry, Jilin University, Changchun, 130012, PR China
[c] Jilin Provincial Key Laboratory of Tooth Development and Bone Remodeling, Changchun, 130021, PR China
[d] School and Hospital of Stomatology, China Medical University, Shenyang, PR China
[e] Key Laboratory of Sustained and Advanced Functional Materials, College of Chemistry, Northeast Normal University, Changchun 130024, PR China
[f] Australian Institute for Bioengineering and Nanotechnology, the University of Queensland, Brisbane, QLD 4072, Australia

ARTICLE INFO

Keywords:
Inflammatory osteolysis
Osteoclastogenesis inhibition
Inflammatory microenvironment
Macrophage reprogramming
Drug repurposing

ABSTRACT

Inflammatory osteolysis poses a significant worldwide threat to public health. However, current monotherapies, which target either the prevention of the inflammatory response or the attenuation of osteoclast (OC) formation, have limited efficacy due to the complexity of the bone immune system being overlooked. Herein, by means of modifying salmon calcitonin (sCT), a multifunctional nano-system (AuNDs-sCT) was designed to synergistically inhibit OC differentiation and reverse the inflammatory microenvironment against inflammatory osteolysis. On the one hand, AuNDs-sCT effectively restrained OC differentiation by binding to the calcitonin receptors on the surface of OC precursors, resulting in the down-regulation of OC-specific genes and proteins. The targeted capacity of AuNDs-sCT provided a more durable and precise therapeutic effect. On the other hand, AuNDs-sCT exhibited antioxidant and anti-inflammatory effects, which regulated the polarization "switch" from the pro-inflammatory M1 phenotype to the anti-inflammatory M2 phenotype in macrophages by the inhibition of NF-κB p65 phosphorylation, thereby effectively reversed the local inflammatory microenvironment. Additionally, AuNDs-sCT served as a promising fluorescent probe, enabling real-time visualization of the therapeutic process. This capability is expected to optimize drug administration and evaluate therapeutic effects. In summary, by inhibiting OC differentiation and reprogramming macrophages, AuNDs-sCT successfully realized drug repurposing and achieved the "one arrow two eagles" therapeutic strategy, which offers a synergistic and effective treatment option for the clinical management of inflammatory osteolysis.

1. Introduction

Inflammation plays a crucial role in disrupting bone homeostasis, leading to various inflammatory osteolytic diseases, such as rheumatoid arthritis, periodontal disease, and orthopedic implant-associated osteolysis [1,2]. These diseases lead to a range of complications, including hypercalcemia, pain, and even pathological fractures, posing a severe worldwide threat to public health and causing enormous social and economic repercussions [3]. In addition to the extensive inflammatory responses, the excessive or hyperactive osteoclasts (OCs) directly contribute to osteolytic processes. Clinically, drugs such as denosumab, which attenuates excessive OC formation, arrest the progression of inflammatory osteolysis [4]. However, due to the combined effects of overactive inflammation and osteoclastic bone resorption, such monotherapies must be accompanied by anti-inflammatory agents in these disorders. Unfortunately, prolonged use of anti-inflammatory drugs can

* Corresponding author. Department of Oral Pathology, Hospital of Stomatology, Jilin University, Changchun, 130021, PR China.
** Corresponding author.
E-mail addresses: linquan@jlu.edu.cn (Q. Lin), ceshi@jlu.edu.cn (C. Shi).
[1] Tong Sha and Ze Wang contributed equally to this work.

https://doi.org/10.1016/j.mtbio.2024.101285
Received 19 July 2024; Received in revised form 12 September 2024; Accepted 1 October 2024
Available online 5 October 2024

lead to drug resistance. Therefore, exploring novel approaches that simultaneously inhibit OC differentiation and reverse the inflammatory microenvironment are pivotal therapeutic strategies to improve the poor prognosis of inflammatory osteolysis.

Inflammatory osteolysis has multiple etiologies. Nonetheless, regardless of the cause or cellular contexts, OCs are the principal bone-resorptive cells involved in bone destruction [5]. OCs are multinucleated cells derived from the monocyte-macrophage lineage. In the presence of macrophage colony-stimulating factor (M-CSF) and receptor activator of nuclear factor-κB ligand (RANKL), OC precursors recruit the adapter protein TNF receptor-associated factor (TRAF) 6 in the cytoplasm, triggering various intracellular signaling cascades [6]. Eventually, this process promotes OC differentiation, survival, and bone resorption by upregulating the expressions of OC-specific genes and proteins. Typically, OCs are in an excessive or hyperactive state at the sites of inflammatory osteolysis, exerting a direct and uppermost role in bone destruction during this process. Thus, inhibiting OC differentiation and bone resorption capability is the foundation for the treatment of inflammatory osteolysis.

In the bone microenvironment, immune cells are increasingly recognized for their ability to interact with bone cells and regulate bone homeostasis. Traditional studies have focused only on individual factors, neglecting the complexity of the bone immune system, thus limiting therapeutic effects. Among these immune cells, circulating monocytes can selectively migrate to inflamed sites, where they differentiate into resident macrophages, thereby exacerbating the inflammatory response [7]. Macrophages are crucial effector immune cells in inflammatory osteolysis due to their dual functionality as principal sources of inflammatory cytokines and their potential to differentiate into OCs [8]. Macrophages can be broadly classified into two major phenotypes (M1 and M2) based on their polarization states [9]. Upon exposure to specific inflammatory stimuli such as lipopolysaccharide (LPS), macrophages are induced to adopt a pro-inflammatory M1 phenotype [10,11]. The secreted pro-inflammatory cytokines, in turn, could induce OC differentiation [12]. In contrast, M2 macrophages suppress inflammation and repair inflammation-associated injuries [13]. Studies have shown that interleukin (IL)-10, secreted by M2 macrophages, can inhibit osteoclastogenesis by suppressing nuclear factor of activated T-cells 1 (NFATc1) [12]. In summary, macrophages and their secreted cytokines not only determine the inflammatory microenvironment but also interact with OCs, thereby governing bone homeostasis through complex mechanisms and crosstalk. Given the critical role of macrophage polarization states in inflammatory osteolysis, it is equally imperative to induce macrophage differentiation from the pro-inflammatory M1 phenotype to the anti-inflammatory M2 phenotype and to inhibit osteoclastogenesis for the effective treatment of inflammatory osteolysis.

Calcitonin (CT) is a well-established anti-resorptive agent, known for its ability to reduce serum calcium levels and inhibit the bone resorption activity of OCs. OCs prominently express CT receptors (CTRs) on their cell membrane, and upon binding to CT, their bone resorption activity ceases within a few minutes [14]. Specifically, the ruffled borders (active sites of bone resorption) of OCs disappear, and OCs detach from the bone surface [15]. Additionally, CTRs are also expressed on mononucleated OC progenitors in late differentiation stages, indicating the potential of CT to simultaneously intervene in both OCs and OC precursors. Among the various CT species, salmon calcitonin (sCT) has been widely used due to its highest intrinsic potency (40–50 times greater than human CT), which translates to superior efficacy and favorable safety [16]. Moreover, sCT has been clinically employed in the treatment of postmenopausal osteoporosis [17], further demonstrating its robust anti-resorptive effects. However, sCT alone does not ameliorate the inflammatory response or exert immunomodulatory effects to promote M2 macrophage differentiation, thereby limiting its application in inflammatory osteolysis. Leveraging the concept of "drug repurposing", which repurposes existing drugs for novel therapeutic purposes [18,19]. Exploiting novel approaches to modify sCT and endowing it with novel anti-inflammatory functions will present an appealing proposition for the treatment of inflammatory osteolysis, potentially offering reduced overall development costs and shorter development timelines.

Recently, the application of nanomaterials has garnered significant attention as a novel approach for disease diagnosis, monitoring, and treatment. Among these nanomaterials, gold nanoparticles (AuNPs) have attracted considerable interests due to their unique properties, including ultra-small size and biocompatibility in physiological environments. The facile surface functionalization of AuNPs makes them an excellent carrier for linking targeted fragments, such as antibodies and peptides, as well as therapeutics drugs [20]. The conjugation of AuNPs with drug molecules also plays an important role in the treatment of inflammatory osteolysis, opening avenues for "drug repurposing". It has been verified that the use of Au delivery systems effectively enhances therapeutic efficacy and reduces side effects in the treatment of RA and other inflammatory diseases [21–23]. Importantly, AuNPs have the ability to inhibit inflammatory cytokines, such as tumor necrosis factor (TNF)-α and IL-1β, thereby exhibiting significant anti-inflammatory effects [24]. Furthermore, AuNPs possess immunomodulatory properties capable of regulating the polarization of macrophages from a pro-inflammatory M1 phenotype to an anti-inflammatory M2 phenotype, thereby alleviating inflammation [25]. In addition, AuNPs exhibit excellent optical properties, making them suitable for fluorescence (FL) imaging [26]. This feature could be useful for visualizing the retention and distribution of drugs within the body, facilitating the tracking of therapeutic effects. Therefore, the combination of AuNPs with sCT holds promise for achieving "drug repurposing" and effectively addressing inflammatory osteolysis through a "one arrow two eagles" therapeutic strategy.

In this study, we designed a multifunctional gold nanodots-sCT (AuNDs-sCT) to target OC precursors, thereby inhibiting OC differentiation and reversing the inflammatory state by reprogramming macrophages (Scheme 1). Glutathione (GSH), a ubiquitous antioxidant pivotal in intracellular redox homeostasis and oxidative stress prevention, served as the ligand for synthesizing biocompatible and ultra-small AuNDs through an electrochemical exchange method. Subsequently, sCT was conjugated to the AuNDs via an amidation reaction. By employing a "one arrow two eagles" therapeutic strategy, the designed AuNDs-sCT exhibited promising efficacy in managing inflammatory osteolysis. Through the specific binding between sCT and CTRs, AuNDs-sCT anchored at the sites of inflammatory osteolysis, ensuring sustained and precise therapeutic effects. On the one hand, AuNDs-sCT targeted the CTRs on OC precursors, inhibiting OC differentiation and bone resorption. Treatment with AuNDs-sCT resulted in the downregulation of OC-specific genes, including *Nfatc1*, *Traf6*, *Fos*, *Dcstamp*, *Acp5*, *Mmp9*, and *Ctsk*, as along with the inhibition of the protein expressions of matrix metalloproteinase 9 (MMP9) and cathepsin K (CTSK). On the other hand, AuNDs-sCT demonstrated excellent anti-inflammatory properties by reprogramming pro-inflammatory M1-type macrophages into anti-inflammatory M2-type macrophages. AuNDs-sCT inhibited NF-κB p65 phosphorylation, resulting in decreased release of pro-inflammatory factors and increased release of anti-inflammatory factors, ultimately reversing the inflammatory microenvironment at the sites of inflammatory osteolysis. Moreover, AuNDs-sCT exhibited favorable fluorescence properties, enabling its use as a visualized probe for drug administration, facilitating precise control over drug delivery. Collectively, AuNDs-sCT provided a precise treatment approach for the clinical management of inflammatory osteolysis, realizing a novel application of traditional drugs.

2. Materials and methods

2.1. Materials

Glutathione (GSH) and chloroauric acid ($HAuCl_4$) were purchased

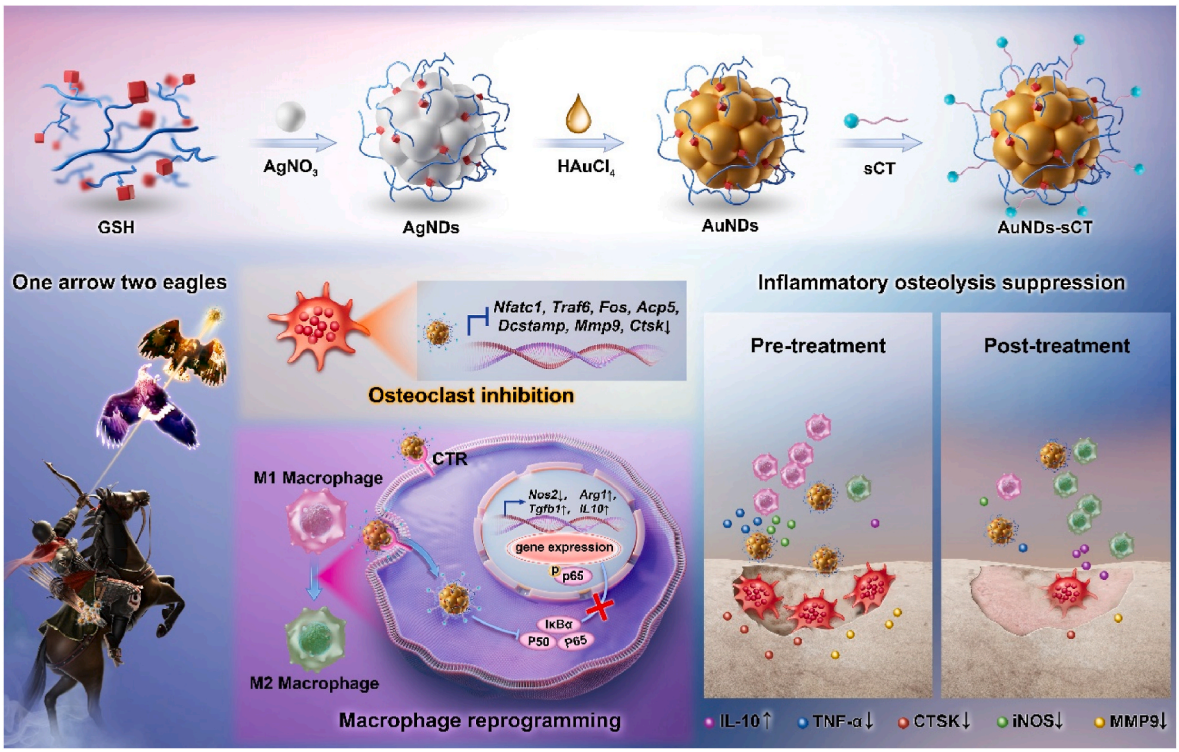

Scheme 1. Multifunctional nano-system AuNDs-sCT was designed for inhibiting osteoclast differentiation and reversing inflammatory microenvironment against inflammatory osteolysis.

from Aldrich. Silver nitrate ($AgNO_3$), hydrazine hydrate ($N_2H_4{\cdot}H_2O$), and isopropyl alcohol were purchased from Sinopharm Group Chemical Reagent Co., LTD. Sodium hydroxide (NaOH) was purchased from Beijing Chemical Plant. N-hydroxysuccinimide (NHS) and N-(3-(dimethylamino)propyl)-N-ethylcarbodiimide hydrochloride (EDC) were purchased from Aladdin. sCT was bought from MeilunBio (MB1213). All reagents were not further treated, and the water used throughout the experiment was secondary deionized water (18.2 MΩ × cm^{-1}).

2.2. Preparation of AgNDs

109.9 mg $AgNO_3$ and 199.5 mg GSH were weighed and dissolved in 10 mL secondary deionized water. The mixture was gently stirred at room temperature for 30 min to ensure even dissolution, resulting in the formation of a milky Ag-GSH gel. To adjust the pH to 6–7, an appropriate amount of NaOH (1 M) was added to the solution, causing the milky gel to transform into a clear and transparent solution. Then, 1 mL hydrazine hydrate was added as a reducing agent, and the solution was stirred at room temperature, protected from light, for 48 h. After 48 h, the product turned into a clear orange-red solution, indicating the formation of AgNDs. The product was then centrifuged at 8800 rpm for 15 min, and the supernatant was filtered to remove impurities. Excess isopropyl alcohol was added to the solution, followed by centrifugation at 6800 rpm for 10 min, and the resulting precipitate was dissolved in 5 mL secondary deionized water.

2.3. Preparation of AuNDs

500 μL AgNDs solution and 250 μL $HAuCl_4$ (50 mM) solution were added successively in 5 mL secondary deionized water. Then an appropriate amount of NaOH (1 M) solution was added to adjust the pH of the solution to 7–9. The mixture was continuously stirred for 4 h at 80 °C. Afterward, the product was centrifuged at 8800 rpm for 15 min, and the supernatant was treated with excess isopropyl alcohol before undergoing another centrifugation at 8000 rpm for 8 min. The resulting precipitate obtained by centrifugation was dissolved in 5 mL secondary deionized water, and the yielding light-yellow transparent solution contained AuNDs.

2.4. Preparation of AuNDs-sCT

To prepare AuNDs-sCT, 2 mL of the previously prepared AuNDs solution was combined with 6.4 mg EDC and 3.2 mg NHS. The mixture was stirred at room temperature for 30 min. Then 100 μL sCT solution was added, and the solution was incubated at room temperature for 8 h. After dialysis for 12 h, AuNDs-sCT solution was obtained.

2.5. Characterization

Transmission electron microscope (TEM) images were taken by a JEOL TECNAI F20 field emission electron microscope with the operating voltage of 200 kV. Fourier transform infrared (FTIR) spectra of the samples were measured by a Nicolet Avatar 360 Fourier transform infrared spectrometer. The Zeta potential of the samples was measured by a Zetasizer Nano ZS particle size analyzer. The UV–visible absorption spectra were obtained by a Lambad 800 UV–visible spectrophotometer. The fluorescence spectra were measured using a Shimadzu RF-5301 PC fluorescence spectrometer. X-ray photoelectron spectra were measured by a VG ESCALAB MKII spectrometer.

2.6. Cell culture

RAW264.7 cells was obtained from the Hospital of Stomatology, Jilin University. The cells were cultured in Dulbecco's modified Eagle's medium (DMEM, Sigma) supplemented with 10 % fetal bovine serum (FBS, Clark Bioscience, Shanghai, China) at 37 °C in a humidified atmosphere containing 5 % CO_2.

To obtain murine bone marrow-derived monocytes/macrophages (BMMs), bone marrow cells were harvested from the femurs and tibiae of female C57BL/6J mice (6 weeks old). The harvested cells were

incubated in complete medium consisting of α-minimal Eagle's medium (α-MEM, Gibco), supplemented with 10 % FBS and 1 % penicillin-streptomycin solution, for 36 h. The non-adherent cells were then collected and incubated in medium containing 20 ng/mL recombinant murine M-CSF (315-02, Peprotech). After incubating for 5 days, the adherent BMMs were obtained for subsequent experiments.

2.7. In vitro biocompatibility assay

RAW264.7 cells and BMMs were seeded in 96-well plates at a density of 1×10^4 cells per well and incubated overnight. The medium was then replaced with fresh medium containing varying concentrations of AuNDs and AuNDs-sCT (0, 5, 50, 100, 200, and 300 μg/mL). After incubation for different times (1 d, 3 d, and 5 d), 10 μL of CCK-8 (Invigentech, USA) was added to each well, and the cells were further incubated for 2 h at 37 °C. The absorbance at 450 nm was detected using a versatile microplate detection system (Synergy™ HT, BioTek). The relative cell viability was calculated using the formula: $(OD_{sample}\text{-}OD_{blank})/(OD_{control}\text{-}OD_{blank}) \times 100$ %. All experiments were independently repeated 3 times.

2.8. Detection of calcitonin receptors (CTRs)

To detect the expression of CTRs, RAW264.7 cells and BMMs were seeded on glass coverslips in 24-well plates and incubated overnight. Then the cells were fixed with 4 % paraformaldehyde and permeabilized with Triton X-100. Following this, the cells were incubated with rabbit anti-calcitonin receptor antibody (1:100, bs-10516R, Bioss) overnight at 4 °C, followed by incubation with CoraLite594-conjugated goat anti-rabbit IgG (1:200, SA00013-4, Proteintech) for 2 h at room temperature. Nuclear staining was performed with DAPI for 5 min at room temperature. CTR expression was detected using a Confocal Laser Scanning Microscope (CLSM).

2.9. Endocytosis of AuNDs and AuNDs-sCT

Cellular uptake of AuNDs and AuNDs-sCT was evaluated by CLSM and flow cytometry. RAW264.7 cells and BMMs were seeded in 24-well plates at a density of 1×10^5 cells per well and incubated overnight. Then, 200 μg/mL AuNDs or AuNDs-sCT solution was added to the cells. After co-culture for 12 h, the culture medium was discarded, and the cells were washed three times with warm phosphate buffer solution. After that, the cells were fixed with 4 % paraformaldehyde and stained with DAPI. Finally, cellular uptake was measured by CLSM and flow cytometry (MACSQuant® Analyzer, Germany). The results were analyzed using FlowJo V10.8.1 software and ImageJ.

2.10. In vivo fluorescence imaging

The protocols involving animal use were reviewed and approved by the Institutional Review Board and Institutional Animal Care and Use Committee of the College of Basic Medical Sciences, Jilin University (Approval No. 2023-601). A murine model of LPS-induced inflammatory osteolysis was constructed in the calvaria of male ICR mice aged 8 weeks. To evaluate the *in vivo* distribution of AuNDs and AuNDs-sCT, a subcutaneous injection of the nanoparticles was administered at a dosage of 10 mg/kg body weight. At 0, 10, 20, 30, 40, 50, 60, 70, and 80 min after injection, the mice were subjected to FL imaging. 2 h after injection, the mice were sacrificed, and the major organs (heart, liver, spleen, lung, and kidney) were collected. Then, the major organs were also detected by FL imaging. Finally, the fluorescence intensity was quantified to assess the distribution and the intensity of the nanoparticles within the tissues.

2.11. Osteoclastogenesis assay and F-actin staining

RAW264.7 cells and BMMs were prepared and cultured as previously described. BMMs were seeded in 96-well plates at a density of 10^4 cells per well. To induce OC formation, 20 ng/mL M-CSF and 50 ng/mL recombinant murine sRANK Ligand (315-11, Peprotech) were added in complete media. Meanwhile, RAW264.7 cells were seeded in 96-well plates at a density of 1500 cells per well and incubated for 6 days in medium containing 50 ng/mL RANKL. Concurrently, varying concentrations of AuNDs-sCT (0, 5, 50, 100, and 200 μg/mL) were added. After 6 days of culture, the cells were fixed.

For TRAP staining, a staining solution containing Sodium Tartrate dihydrate (228729, Sigma), Sodium Acetate (S2889, Sigma), Naphthol ASMX Phosphate disodium salt (N5000, Sigma), and Fast Red Violet (F3381, Sigma) was used to identify OCs. OCs were defined as TRAP-positive multinucleated cells with three or more nuclei. The number of OCs was counted under a 10 × objective lens using a bright-field microscope (Olympus).

For F-actin staining, the cells were permeabilized with 0.5 % Triton-X and incubated with TRITC Phalloidin (CA1610, Solarbio) for 30 min at room temperature, protected from light. Nuclei were counterstained with DAPI. F-actin ring formation was detected under a fluorescence microscope (Olympus), and both the number and area of the actin ring of OCs were quantified.

2.12. Real-time qRT-PCR assay

To detect the expressions of inflammatory-related genes, RAW264.7 cells were incubated with normal medium, LPS (100 ng/mL), or LPS (100 ng/mL) + AuNDs-sCT (200 μg/mL) for 24 h.

To detect the expressions of OC-specific genes, RAW264.7 cells were incubated with RANKL (50 ng/mL), RANKL (50 ng/mL) + AuNDs-sCT (100 μg/mL), or RANKL (50 ng/mL) + AuNDs-sCT (200 μg/mL) for 6 days until OCs were formed.

Total RNA was isolated and extracted using TRIzol reagent (Takara). Then the extracted RNA was reverse transcribed into cDNA, followed by real-time qRT-PCR. The primer sequences were shown in Table 1. The $2^{-\Delta\Delta CT}$ method was used to calculate the relative gene expressions, and all values were normalized to the expression of the housekeeping gene *Actb*.

2.13. Western blot analysis

To detect the expressions of OC-associated proteins, RAW264.7 cells were seeded in 6-well plates at a density of 4.5×10^4 cells per well and incubated with normal medium, RANKL (50 ng/mL), or RANKL (50 ng/mL) + AuNDs-sCT (200 μg/mL) for 6 d.

To detect the expressions of inflammation-related proteins, RAW264.7 cells were seeded in 6-well plates at a density of 5×10^5 cells per well and incubated for 24 h.

Total protein was extracted by lysing the cells on ice for 30 min using radioimmunoprecipitation assay (RIPA) buffer. The proteins were then separated by 10 % sodium dodecyl sulfate-polyacrylamide gel electrophoresis (SDS-PAGE) and transferred to a polyvinylidene fluoride (PVDF) membrane. After blocking the membrane with blocking buffer (5 % skim milk), it was incubated with the primary antibody overnight at 4 °C. After three washes with tris-buffered saline with Tween 20 (TBST), the membrane was incubated with the secondary antibody for 2 h at room temperature. Finally, the protein bands were observed by an enhanced chemiluminescence kit (PK10001, Proteintech), and the relative grayscale intensities were analyzed using ImageJ software.

2.14. LPS-induced calvarial inflammatory osteolysis

The mice were obtained from Beijing Vital River Laboratory Animal Technology Co., Ltd. and randomly divided into three groups: (1) PBS

Table 1
Primer sequences for qRT-PCR.

Genes	Forward (5′–3′)	Reverse (5′–3′)
Nfatc1	CCCGTCACATTCTGGTCCAT	CAAGTAACCGTGTAGCTGCACAA
Traf6	GCTCAAACGGACCATTCGGA	GGGATTGTGGGTCGCTGAAA
Fos	CCAGTCAAGAGCATCAGCAA	AAGTAGTGCAGCCCGGAGTA
Dcstamp	AAAACCCTTGGGCTGTTCTT	AATCATGGACGACTCCTTGG
Acp5	CAAGAACTTGCGACCATTGTTA	ATCCATAGTGAAACCGCAAGTA
Mmp9	GCCCTGGAACTCACACGACA	TTGGAAACTCACACGCCAGAAG
Ctsk	CACCCAGTGGGAGCTATGGAA	GCCTCCAGGTTATGGGCAGA
Nos2	ACTCAGCCAAGCCCTCACCTAC	TCCAATCTCTGCCTATCCGTCTCG
Tnf	TTGAGATCCATGCCGTTG	GCTTGTCACTCGAATTTTGAGA
Tgfb1	GCCCTGGATACCAACTATTGC	GCAGGAGCGCACAATCATGTT
Arg1	CAAGACAGGGCTCCTTTCAG	GTAGTCAGTCCCTGGCTTATGG
Il10	CTGGACAACATACTGCTAACCG	GGGCATCACTTCTACCAGGTAA
Actb	TGGAATCCTGTGGCATCCATGAAAC	TAAAACGCAGCTCAGTAACAGTCCG

group, (2) LPS (5 mg/kg body weight) group, and (3) LPS (5 mg/kg body weight) + AuNDs-sCT (10 mg/kg body weight) group. The injections were administered into the sagittal midline of the calvaria using an insulin syringe on alternate days. After 7 days of treatment, the mice were euthanized, and the calvarias along with vital organs (heart, liver, spleen, lung, and kidney) were collected for further analysis. The bone volume ratio (BV/TV) was analyzed using a micro-CT system.

2.15. Histological examination

The fixed mouse calvarias were immersed in 15 % EDTA solution for 4 weeks. Subsequently, both the calvarias and the vital organs were

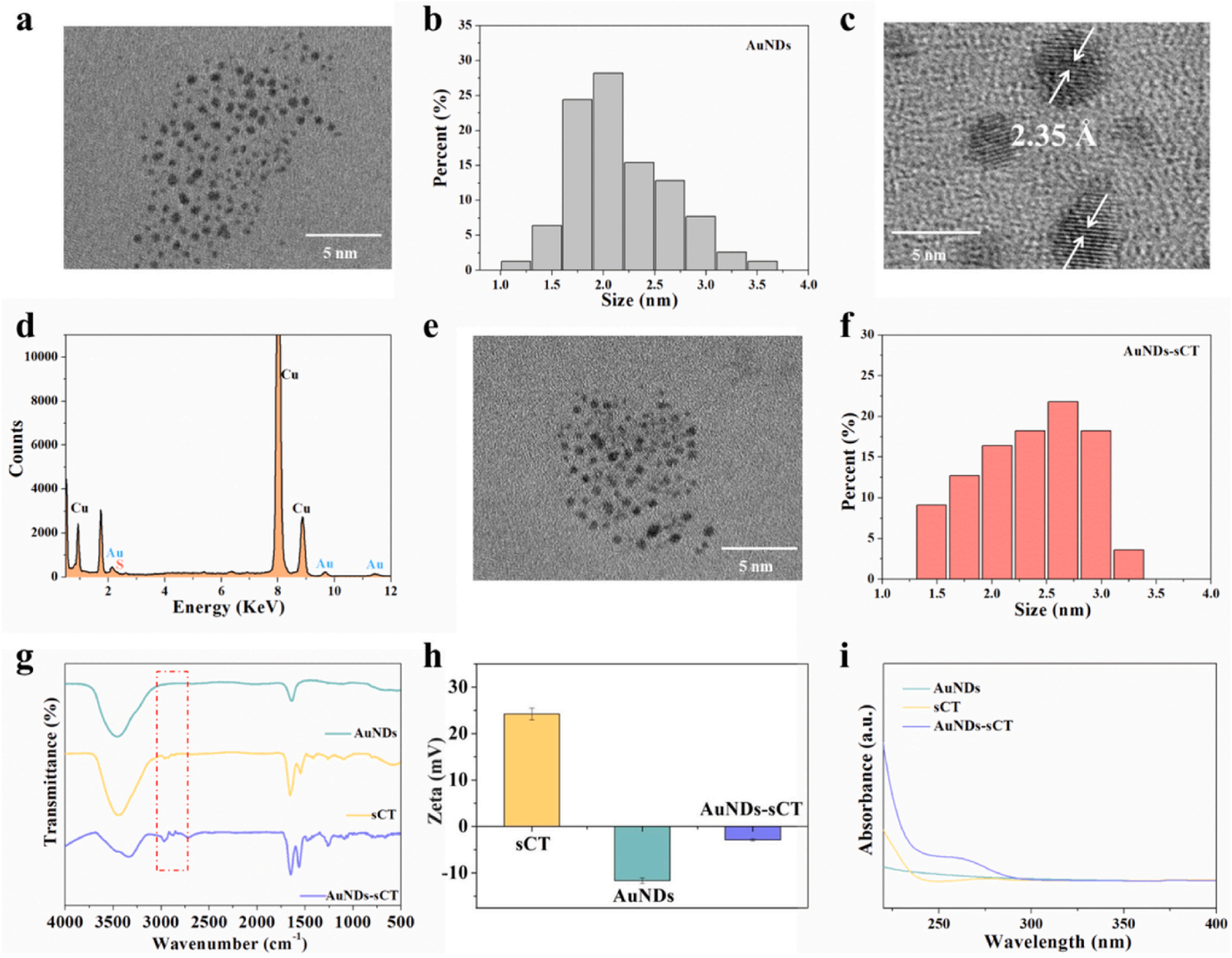

Fig. 1. Characterization of AuNDs-sCT nano-system. (a) TEM image and (b) size distribution histogram of the AuNDs. (c) HRTEM image of AuNDs, showing a crystal lattice spacing of 0.235 nm. (d) Energy-dispersive spectroscopy (EDS) spectrum of AuNDs. (e) TEM image and (f) size distribution histogram of the AuNDs-sCT. (g) FT-IR spectra, (h) zeta potential, and (i) UV spectra of AuNDs, sCT and AuNDs-sCT (n = 3).

embedded in paraffin and sectioned. HE staining, TRAP staining, and immunofluorescence staining were performed on the sections.

2.16. Statistical analysis

Data were shown as mean ± standard deviation (SD). Statistical analyses were performed using one-way ANOVA or Student's *t*-test, and $P < 0.05$ was considered statistical significance.

3. Results and discussion

3.1. Characterization of AuNDs-sCT nano-system

To enhance the efficacy of clinical treatments for inflammatory osteolysis, which are currently limited by a focus on either preventing the inflammatory response or attenuating OC differentiation, we developed a multifunctional nano-system AuNDs-sCT. This system is designed to simultaneously inhibit OC differentiation and reverse the inflammatory microenvironment (Scheme 1). Firstly, gold nanodots (AuNDs) with ultra-small size and excellent biocompatibility were prepared using the electrochemical exchange method. The AuNDs were then conjugated with sCT through an amidation reaction to obtain AuNDs-sCT. We investigated the morphology of the materials, as shown in Fig. 1a and b, which showed that the AuNDs exhibited a good spherical morphology with an average diameter of approximately 2.2 nm. The high-resolution transmission electron microscope (HRTEM) image indicated that the lattice spacing of AuNDs was 0.235 nm (Fig. 1c), consistent with the (111) lattice spacing of face-centered cubic Au [27]. Energy-dispersive spectroscopy (EDS) spectrum analysis confirmed the presence of Au and S elements within the AuNDs (Fig. 1d). After conjugating with sCT, AuNDs-sCT retained its spherical shape, with a slight increased in size to 2.3 nm (Fig. 1e and f). The ultra-small size of AuNDs was a key factor for the fluorescence, which diminished as the size of AuNDs increased.

Next, we analyzed the structure of the materials. The infrared spectrum revealed the absence of characteristic peaks at 2970 and 2876 cm^{-1} for AuNDs, whereas AuNDs-sCT exhibited distinct peaks at these positions, attributable to the methyl group, indicating the successful conjugation of AuNDs with sCT (Fig. 1g). Zeta potential analysis (Fig. 1h) demonstrated a significant negative charge for AuNDs (−11.67 ± 0.57 mV), which was partially neutralized upon conjugation with sCT to −2.88 ± 0.23 mV, with sCT alone exhibiting a charge of 24.23 ± 1.25

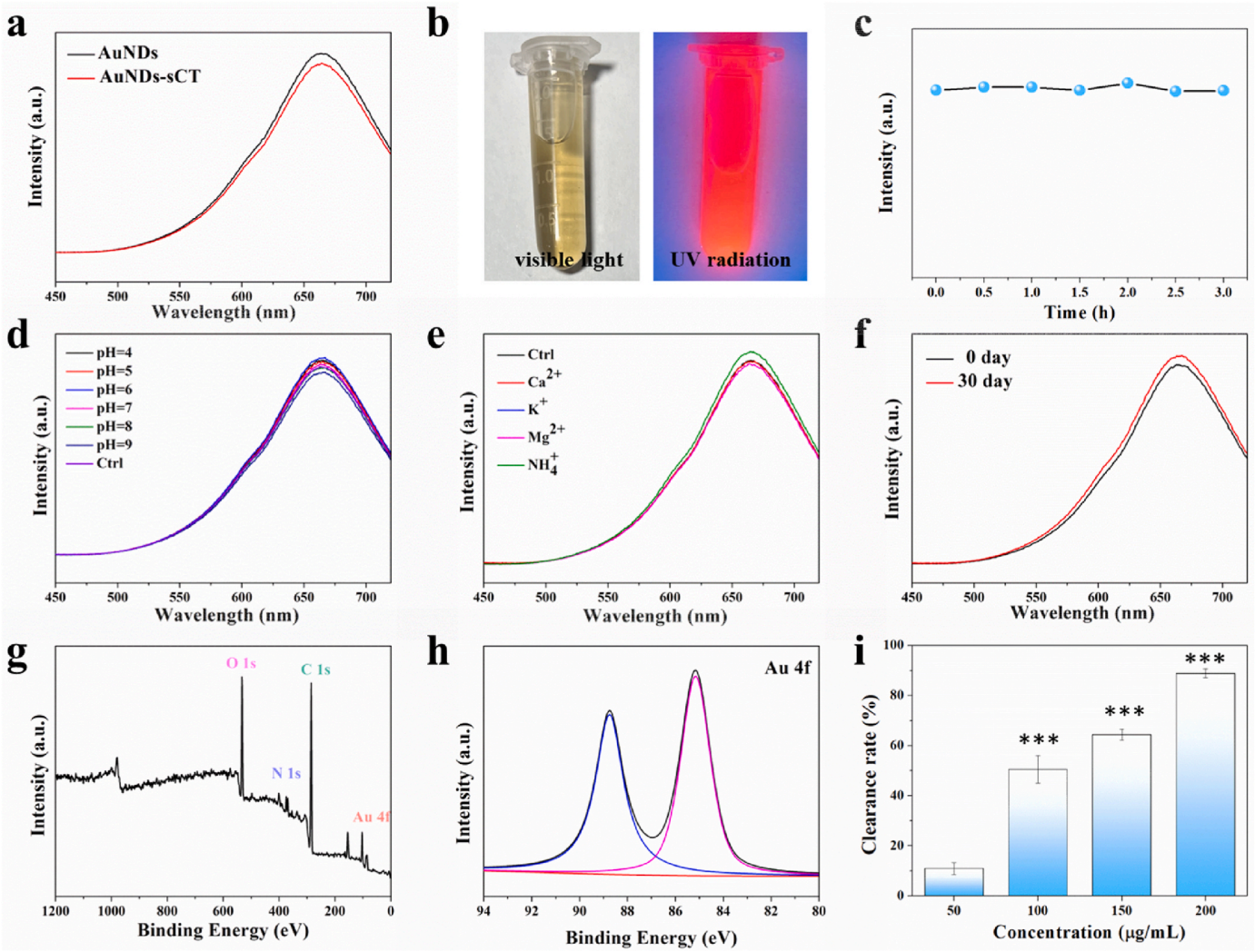

Fig. 2. Fluorescence properties, XPS analysis, and ROS scavenging ability of AuNDs-sCT nano-system. (a) Fluorescence spectra of AuNDs and AuNDs-sCT. (b) The photographs of AuNDs-sCT under visible light and UV-365 nm. (c) Fluorescence intensity of AuNDs-sCT exposed under UV light for various time spans. Fluorescence intensity of AuNDs-sCT at (d) different pH values, (e) high concentrations of interfering ions (Ca^{2+}, K^{+}, Mg^{2+}, NH_4^{+}, 200 mM), and (f) storage under normal conditions for 30 days. (g) XPS survey spectrum of AuNDs-sCT. (h) High-resolution XPS spectra of Au 4f of AuNDs-sCT. (i) ROS scavenging evaluation of AuNDs-sCT at different concentrations through the DPPH approach (n = 3). $^{*}P < 0.05$, $^{**}P < 0.01$, $^{***}P < 0.001$.

mV. In addition, the UV absorption spectrum of the materials was investigated. As shown in Fig. 1i, the AuNDs had no characteristic absorption peaks in the range of 200–400 nm, while sCT exhibited a characteristic absorption peak at 276 nm. After conjugation with sCT, AuNDs-sCT displayed a corresponding absorption peak at 276 nm, indicative of the characteristic absorption of sCT. The above data provided evidence for the synthesis of a structurally stable AuNDs-sCT nano-system.

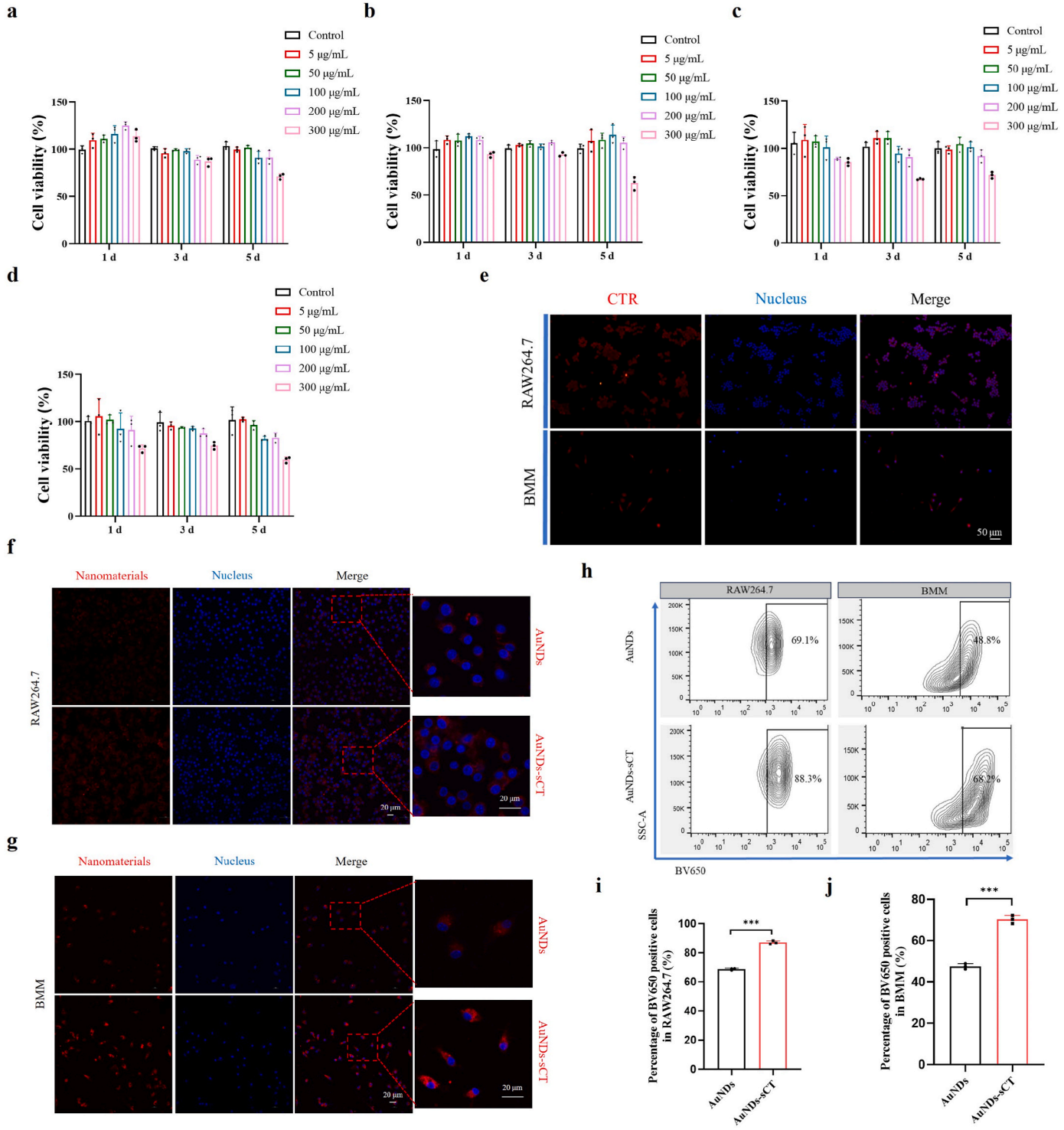

Fig. 3. ***In vitro*** **biocompatibility and targeted property of AuNDs-sCT.** Cell viability of (a) RAW264.7 cells and (b) BMMs after 1, 3, and 5-day exposure to graded concentrations of AuNDs (0, 5, 50, 100, 200, and 300 μg/mL) (n = 3). Cell viability of (c) RAW264.7 cells and (d) BMMs after 1, 3, and 5-d exposure to graded concentrations of AuNDs-sCT (0, 5, 50, 100, 200, and 300 μg/mL) (n = 3). (e) Fluorescence images displaying CTR expression in RAW264.7 cells and BMMs (scale bar: 50 μm). Cellular uptake of AuNDs and AuNDs-sCT (red) in (f) RAW264.7 cells and (g) BMMs using CLSM, with cell nuclei counterstained with DAPI (blue) (scale bar: 20 μm). (h) Flow cytometry analysis of cellular uptake of AuNDs and AuNDs-sCT in RAW264.7 cells and BMMs. Relative quantification of BV650-positive cells in (i) RAW264.7 cells and (j) BMMs (n = 3). $^{*}P < 0.05$, $^{**}P < 0.01$, $^{***}P < 0.001$. (For interpretation of the references to colour in this figure legend, the reader is referred to the Web version of this article.)

Subsequently, we evaluated the fluorescence properties of the AuNDs-sCT. As shown in Fig. 2a, AuNDs exhibited excellent fluorescence emission properties. After connecting sCT, the fluorescence properties of AuNDs-sCT was well-maintained. In visible light, the aqueous solution of AuNDs-sCT appeared yellowish, while under ultraviolet light, it exhibited bright red fluorescence (Fig. 2b). The red fluorescent AuNDs-sCT can serve as an excellent fluorescent probe, holding immense potential for biological labeling and tracing purposes.

The stability of fluorescent probes is very important for both *in vitro* and *in vivo* fluorescence imaging. Therefore, the stability of the fluorescence effect of AuNDs-sCT was tested. Firstly, the photostability was investigated by exposing the AuNDs-sCT solution to ultraviolet light for 3 h. The fluorescence intensity of AuNDs-sCT remained virtually unchanged, with no fluorescence bleaching, signifying excellent photostability (Fig. 2c). Furthermore, the fluorescence stability of AuNDs-sCT over the physiologically relevant pH range of 4–9 was investigated (Fig. 2d). Within this range, the fluorescence intensity of AuNDs-sCT remained stable, indicating excellent pH stability. The ionic stability of AuNDs-sCT in the presence of common cations was investigated. As shown in Fig. 2e, the fluorescence intensity of AuNDs-sCT remained stable even in the presence of high concentrations of interfering ions (Ca^{2+}, K^{+}, Mg^{2+}, NH_4^{+}), indicating excellent ionic stability. In addition, the fluorescence intensity of AuNDs-sCT was well-maintained even after 30 days (Fig. 2f). These findings demonstrated the enduring fluorescence properties of AuNDs-sCT, making it suitable for long-term fluorescence tracing in both *in vivo* and *in vitro* imaging applications.

To evaluate the chemical composition and valence states of the materials, X-ray photoelectron spectroscopy (XPS) was performed. The survey spectrum of AuNDs-sCT exhibited characteristic peaks corresponding to O 1s, N 1s, C 1s, S 2p, and Au 4f (Fig. 2g). In the Au 4f spectrum, the characteristic peaks at 88.8 eV and 85.2 eV confirmed the presence of both Au (0) and Au (I) states in the AuNDs-sCT (Fig. 2h) [28, 29]. The Au (0) is instrumental for nanodot nucleation, while the Au (I) can react with sulfhydryl groups to form stable Au-S bonds. The Au-S bonds not only enhanced the stability of the nanodots but also endowed AuNDs-sCT with bright and stable fluorescence characteristics.

Inflammation is commonly linked to an increased production of reactive oxygen species (ROS) [30]. In order to explore the potential anti-inflammatory mechanisms of AuNDs-sCT, the ability of AuNDs-sCT to scavenge ROS was evaluated using the classical DPPH method. As shown in Fig. 2i, AuNDs-sCT, with L-GSH as the ligand, exhibited concentration-dependent ROS-scavenging activity, indicating its potential for effective antioxidation in both *in vitro* and *in vivo* settings. This characteristic is advantageous for enhancing the anti-inflammatory effects of the nano-system. The excellent anti-inflammatory effect of AuNDs-sCT suggested its promising application in the treatment of inflammatory osteolysis.

3.2. In vitro biocompatibility and targeted capacity of AuNDs-sCT

To assess the biocompatibility of the synthesized AuNDs-sCT with their targeted cells, primary bone marrow-derived monocytes (BMMs) and RAW264.7 cells were used as OC precursors. These cells were exposed to graded concentrations of AuNDs or AuNDs-sCT (0, 5, 50, 100, 200, and 300 μg/mL). As shown, RAW264.7 cells (Fig. 3a) and BMMs (Fig. 3b) maintained a survival rate above 80 % when incubated with concentrations of AuNDs up to 200 μg/mL for 1 d, 3 d or 5 d. Comparable findings were observed after the treatment with AuNDs-sCT (Fig. 3c and d), underscoring the excellent biocompatibility of both AuNDs and AuNDs-sCT. Based on the above findings, a concentration of up to 200 μg/mL was selected for both AuNDs and AuNDs-sCT in subsequent *in vitro* experiments. Considering the specific binding affinity of sCT to calcitonin receptors (CTRs), a member of the 7-transmembrane protein family [31], we firstly assessed the expression of CTRs on the cell surface of RAW264.7 cells and BMMs by immunofluorescence staining. As shown in Fig. 3e, CTRs are extensively expressed on the cell membranes of both cell types. Besides, the designed AuNDs-sCT, with its superior fluorescence properties, enabled the visualization of cellular uptake and targeted delivery by confocal laser scanning microscope (CLSM) and flow cytometry. As shown in Fig. 3f and g, RAW264.7 cells (Fig. 3f) and BMMs (Fig. 3g) exhibited red fluorescence from AuNDs and AuNDs-sCT, along with blue fluorescence from nuclear staining. Interestingly, the AuNDs-sCT group displayed a more intense red fluorescence signal compared to AuNDs group, indicating a specific uptake mechanism by RAW264.7 cells and BMMs, with the differential uptake rates attributed to the targeted interaction between sCT to CTRs. Further, flow cytometry analysis substantiated these observations, revealing a higher uptake rate of AuNDs-sCT in both cell types compared to AuNDs alone (Fig. 3h). Specifically, as shown in Fig. 3i and j, the uptake rate of AuNDs-sCT in RAW264.7 cells remarkably increased from 68.7 ± 0.78 % to 87.0 ± 1.38 % compared to AuNDs, and in BMMs, it increased from 47.5 ± 1.3 % to 70.2 ± 2 %. To sum up, these results indicated that the conjugation of sCT to AuNDs significantly promoted the cellular uptake by RAW264.7 cells and BMMs, laying the foundation for the subsequent inhibition of OC differentiation and macrophage reprogramming.

3.3. In vivo targeted capacity and fluorescence imaging performance

The excellent optical properties of AuNDs and AuNDs-sCT make them ideal candidates for fluorescence (FL) imaging. To further explore the feasibility of AuNDs-sCT as a targeted fluorescent probe for OCs and macrophages in inflammatory osteolysis *in vivo*, FL imaging techniques were performed using a calvarial inflammatory osteolysis model. The results demonstrated that the FL intensity of AuNDs at the site of calvarial inflammation exhibited a transient increase followed by a sharp decline (Fig. 4a and c). In contrast, AuNDs-sCT displayed sustained high FL intensity at the target site for an extended period before it gradually decreased (Fig. 4b and c). Notably, AuNDs-sCT was retained at the site of inflammation for more than 80 min, which significantly improved the therapeutic efficiency to a certain extent. Finally, FL imaging of the major organs revealed the highest FL emission in the kidney and liver for both AuNDs and AuNDs-sCT (Fig. S1). The above results showed that AuNDs-sCT effectively targeted and maintained excellent FL imaging capabilities at the site of calvarial inflammatory osteolysis *in vivo*, which holds considerable significance for precise localization and real-time therapeutic management of inflammatory osteolysis in clinical applications.

3.4. In vitro inhibition of RANKL-induced OC differentiation

The multifunctional AuNDs-sCT nano-system, leveraging the properties of sCT, was expected to exert potent anti-resorptive abilities, thereby addressing one crucial aspect of our “one arrow two eagles” therapeutic strategy in the treatment of inflammatory osteolysis. Firstly, we assessed the effect of AuNDs-sCT on RANKL-induced OC differentiation. RANKL is positively correlated with OC differentiation and bone resorptive function, contributing to osteolysis by favoring exacerbated osteoclast formation and accelerating bone resorption in response to inflammatory cytokines. Specifically, BMMs and RAW264.7 cells were incubated with various concentrations of AuNDs-sCT and concurrently stimulated with RANKL for 6 days. As shown in Fig. 5a and b, a remarkable dose-dependent decrease in the number of tartrate-resistant acid phosphatase (TRAP)-positive multinucleated OCs derived from BMMs was observed when compared to the control group, indicating the inhibitory effects of AuNDs-sCT on OC differentiation from BMMs. Besides, the formation of a dense F-actin ring is a critical step in OC differentiation and is mandatory for the process of bone resorption. Thus, F-actin fluorescence staining was used to determine the effects of AuNDs-sCT on this process (Fig. 5a). The results demonstrated that both the number and size of F-actin rings during osteoclastogenesis were dose-dependently reduced by AuNDs-sCT, further indicating the

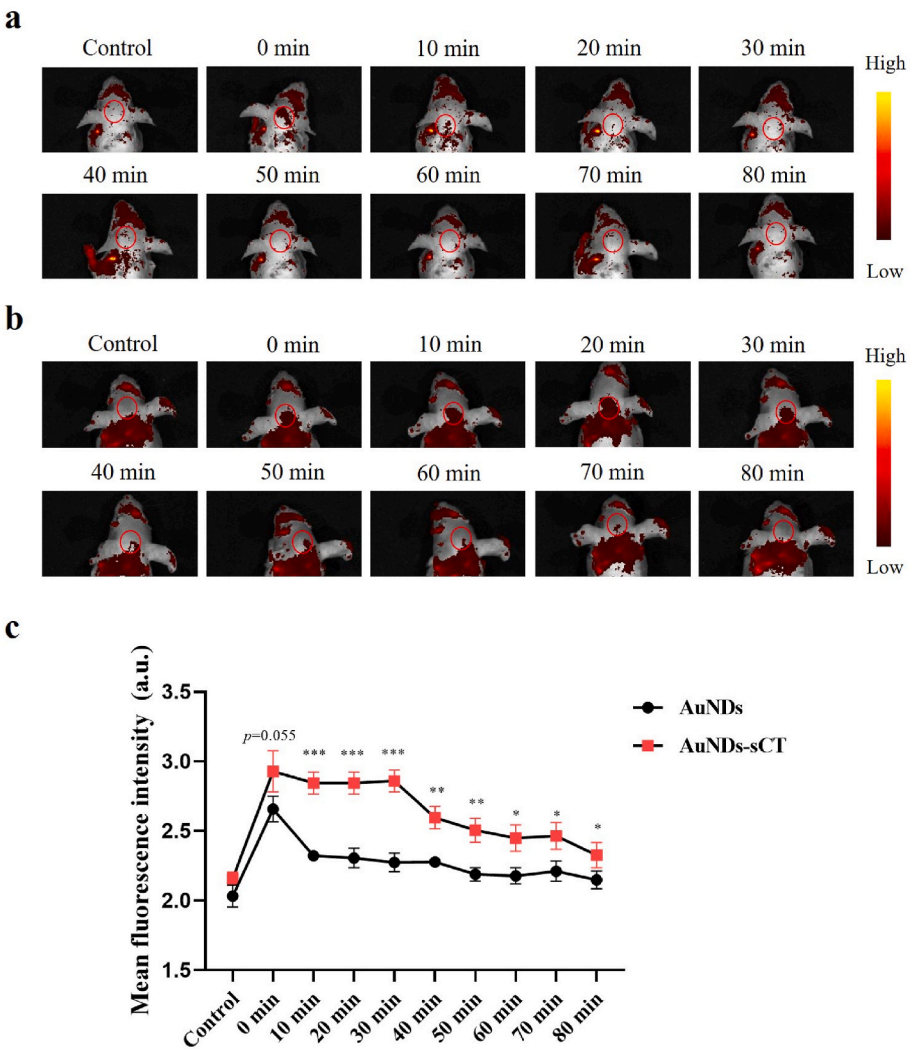

Fig. 4. ***In vivo*** **imaging fluorescence performance of AuNDs-sCT.** (a) FL imaging showcasing the capabilities of AuNDs over time. (b) FL imaging showcasing the capabilities of AuNDs-sCT over time. (c) Quantitative evaluation based on FL imaging data over time following the administration of AuNDs and AuNDs-sCT (n = 3). $^{*}P < 0.05$, $^{**}P < 0.01$, $^{***}P < 0.001$.

inhibition of OC differentiation (Fig. 5c). Furthermore, the OCs derived from BMMs following treatment with AuNDs-sCT were remarkably smaller than those in the control group, suggesting the inhibition of OC differentiation, particularly the fusion process (Fig. 5d). Similar results regarding TRAP-positive multinucleated OCs (Fig. 5e–. f, and Fig. 5h) and F-actin staining (Fig. 5e and g) were verified in RAW264.7 cells. Thus, as OC precursors, both BMMs and RAW264.7 cells derived OCs showed a remarkable reduction in size and number. The above findings firmly validated the dose-dependent inhibitory effect of AuNDs-sCT on RANKL-induced osteoclastogenesis.

Building upon our remarkable outcomes regarding the inhibition of OC differentiation, we further explored the effects of AuNDs-sCT on the expressions of OC-specific genes and proteins in RAW264.7 cells. Using real-time quantitative reverse transcription polymerase chain reaction (qRT-PCR), we detected a dose-dependent downregulation of key OC-specific genes, including *Nfatc1* (Fig. 6a), *Traf6* (Fig. 6b), *Fos* (Fig. 6c), *Dcstamp* (Fig. 6d), *Acp5* (Fig. 6e), *Mmp9* (Fig. 6f), and *Ctsk* (Fig. 6g), upon treatment with AuNDs-sCT especially at a concentration of 200 μg/mL. Based on the above findings, a concentration of 200 μg/mL was selected for AuNDs-sCT in subsequent *in vitro* experiments. These results were also consistent with the results from the TRAP assay and F-actin fluorescence staining (Fig. 5e). As reported, the interaction between RANKL and RANK initiates a cascade of intracellular signaling events, including NF-κB, MAPK, and RANKL-induced calcium oscillations. Among these pathways, the RANKL/RANK/TRAF6 axis is particularly crucial, leading to the robust induction of transcription factors such as *c-Fos* and *NFATc1* [32,33]. In our study, treatment with 200 μg/mL AuNDs-sCT markedly downregulated the mRNA level of *Traf6*, *c-Fos*, and *NFATc1*, all of which play indispensable roles in osteoclast differentiation. It is well-known that OCs contribute to bone erosion by secreting H^{+}, Cl^{-}, cathepsin K (CTSK), and matrix metalloproteinases (MMPs) onto the bone resorption surface [34]. Therefore, we evaluated the protein expressions of MMP9 and CTSK by Western blot assays. Our findings revealed a significant inhibition of MMP9 and CTSK protein expression in the AuNDs-sCT treated group during OC differentiation (Fig. 6h–. i and j), indicating a disruption in the enzymes responsible for bone resorption and a subsequent suppression of bone erosion in inflammatory osteolysis. The above results demonstrated that AuNDs-sCT attenuated the expressions of OC-specific genes and proteins, thereby inhibiting OC differentiation and bone resorption.

3.5. *In vitro phenotype and reprogramming mechanism of macrophages*

The above results demonstrated the potent *in vitro* inhibitory effects of AuNDs-sCT on osteoclastogenesis, a critical process in inflammatory osteolysis. However, merely inhibiting OC differentiation is insufficient

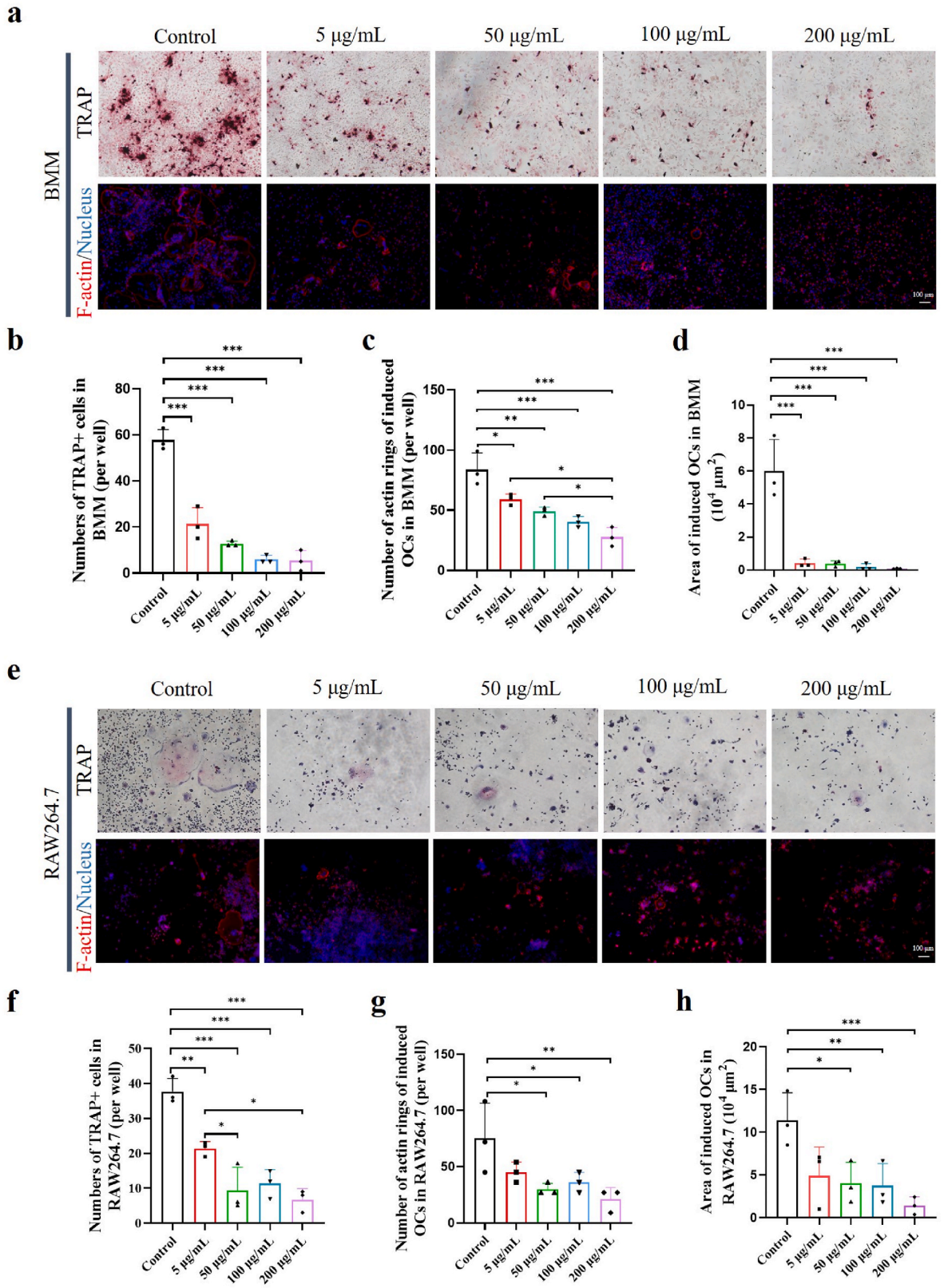

Fig. 5. ***In vitro*** **inhibition of RANKL-induced OC differentiation by AuNDs-sCT in a dose-dependent manner.** (a) Representative images of TRAP staining and F-actin fluorescence staining in RANKL-induced BMMs after 6-day exposure to graded concentrations of AuNDs-sCT (0, 5, 50, 100, and 200 μg/mL). Scale bar = 100 μm. (b) Quantification of TRAP-positive multinucleated cells (≥3 nuclei), (c) number of actin rings, (d) area of induced OCs in BMMs (n = 3). (e) Representative images of TRAP staining and F-actin fluorescence staining in RANKL-induced RAW264.7 cells after 6-day exposure to graded concentrations of AuNDs-sCT (0, 5, 50, 100, and 200 μg/mL). Scale bar = 100 μm. (f) Quantification of TRAP-positive multinucleated cells (≥3 nuclei), (g) number of actin rings, (h) area of induced OCs per well in RAW264.7 cells (n = 3). $^*P < 0.05$, $^{**}P < 0.01$, $^{***}P < 0.001$.

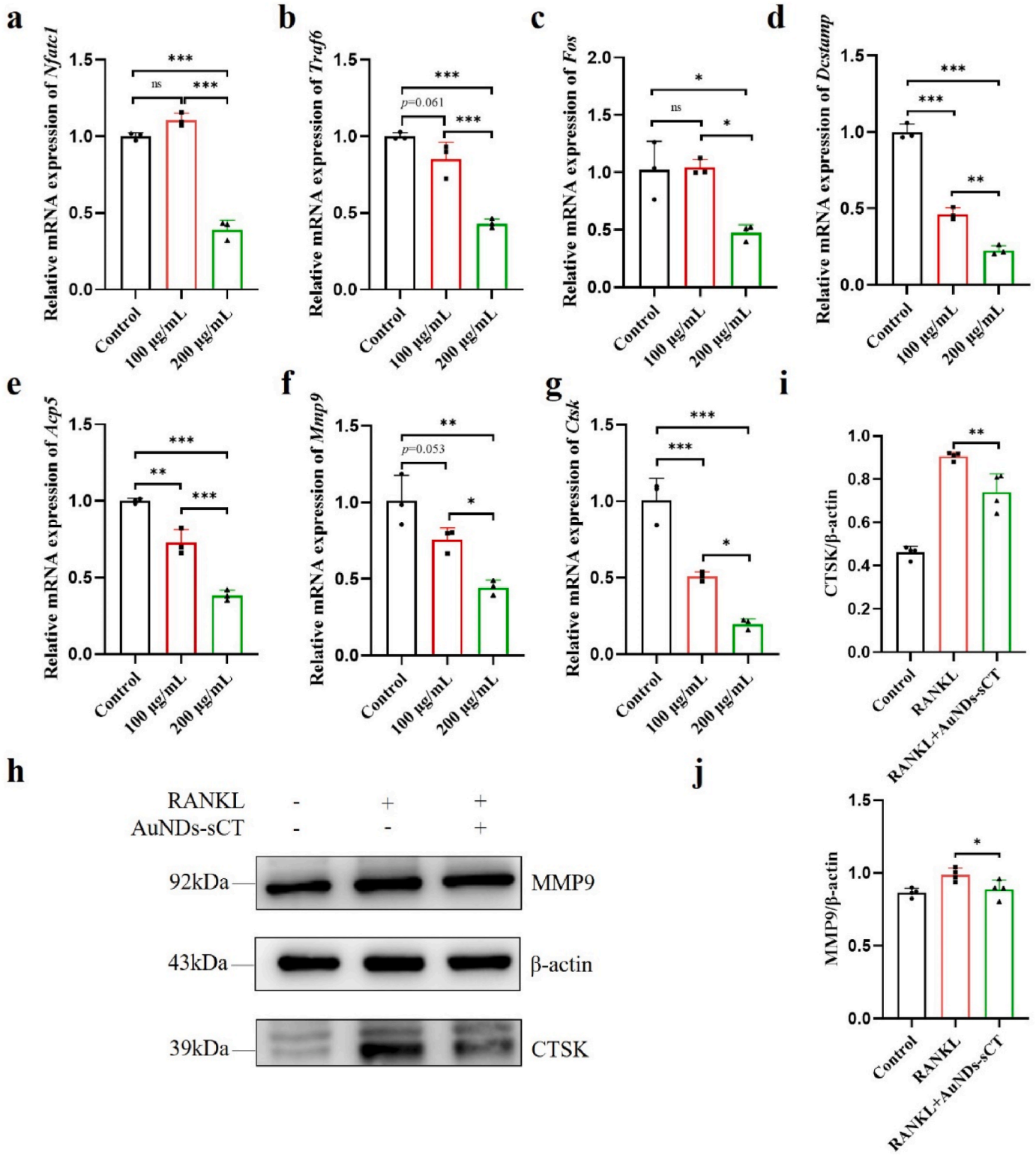

Fig. 6. AuNDs-sCT down-regulated OC-specific genes and proteins. Relative expressions of OC-specific genes, (a) *Nfatc1*, (b) *Traf6*, (c) *Fos*, (d) *Dcstamp*, (e) *Acp5*, (f) *Mmp9*, *and* (g) *Ctsk* in RAW264.7 cells (n = 3). (h) The protein expressions of MMP9 and CTSK were assessed by Western blot. Quantification of (i) MMP9 and (j) CTSK relative to β-actin (n = 4). $^{*}P < 0.05$, $^{**}P < 0.01$, $^{***}P < 0.001$.

for the treatment of inflammatory osteolysis. To address this, AuNDs-sCT must also possess robust anti-inflammatory capabilities, aligning with our "one arrow two eagles" therapeutic strategy. Subsequently, we observed the morphological changes of RAW264.7 cells following treatment with AuNDs-sCT under a microscope. As shown in Fig. 7a, RAW264.7 cells maintained a round morphology when treated with either AuNDs or AuNDs-sCT alone. Conversely, LPS induced a transition to a spindle-like, elongated morphology (as indicated by the black arrows), which is characteristic of M1 macrophages. Notably, treatment with AuNDs or AuNDs-sCT alongside LPS led to a reversion of the

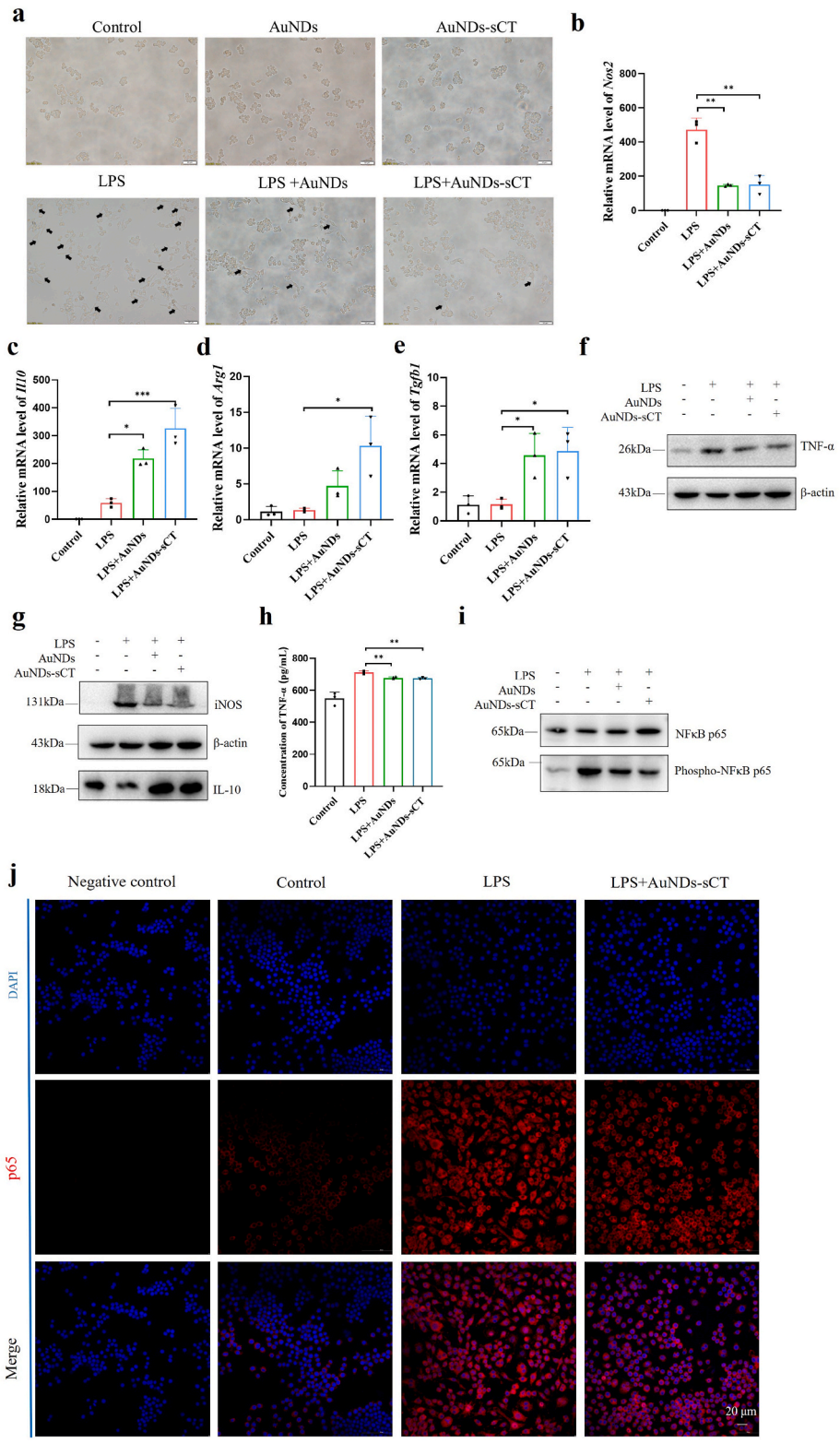

Fig. 7. *In vitro* polarization of macrophages by AuNDs-sCT. (a) Morphology of RAW264.7 cells after 24-h exposure to AuNDs-sCT under a light microscope. The black arrows indicate a spindle-like, elongated morphology. Scale bar = 50 μm. Quantitative qRT-PCR results for (b) *Nos2*, (c) *Il10*, (d) Arg*1*, and (e) *Tgfb1* expression. Western blot analysis of (f) TNF-α, (g) iNOS, and IL-10 protein levels in RAW264.7 cells treated with control, LPS, LPS + AuNDs, and LPS + AuNDs-sCT. (h) ELISA results for TNF-α in cell culture supernatants. (i). Western blotting for NF-κB p65 and Phospho-NF-κB p65. (j) Localization of NF-κB p65 in RAW264.7 cells using confocal laser scanning microscope (CLSM), with cell nuclei counterstained with DAPI (blue). Scale bar = 20 μm (n = 3). $^{*}P < 0.05$, $^{**}P < 0.01$, $^{***}P < 0.001$. (For interpretation of the references to colour in this figure legend, the reader is referred to the Web version of this article.)

elongated shape to a relatively round morphology. This morphological shift indicated that both AuNDs and AuNDs-sCT may have the capacity to modulate the polarization status of macrophages.

To further characterize the polarization status of macrophages treated with AuNDs or AuNDs-sCT, we measured the mRNA expression levels of M1 and M2 macrophage markers and cytokine secretions in RAW264.7 cells. M1 macrophages are characterized by the secretion of pro-inflammatory cytokines including IL-1β, IL-6, inducible nitric oxide synthase (iNOS), and TNF-α, whereas M2 macrophages secrete high levels of anti-inflammatory cytokines including IL-10, arginase 1 (ARG1), and transforming growth factor-β (TGF-β). Among them, iNOS and IL-10 are respective markers for M1 and M2 macrophages [35]. As shown in Fig. 7b and g, LPS stimulation induced RAW264.7 cells towards an M1 phenotype, characterized by an increase in iNOS expression at both the mRNA and protein levels. However, treatment with 200 μg/mL AuNDs or AuNDs-sCT significantly reduced *Nos2* (encoding iNOS) mRNA and iNOS protein levels compared to the LPS group. Correspondingly, AuNDs or AuNDs-sCT treatment led to a significant upregulation of IL-10 mRNA and protein levels compared to the LPS group (Fig. 7c and g), indicative of an M2-associated anti-inflammatory response. In agreement with this, the mRNA levels of Arg*1* and *Tgfb1*, encoding two important anti-inflammatory cytokines ARG1 and TGF-β, were also significantly increased in response to AuNDs or AuNDs-sCT (Fig. 7d and e). Interestingly, while the mRNA levels of *Tnf*, encoding a key protein TNF-α secreted by M1-type macrophages, were not changed after AuNDs or AuNDs-sCT treatment (Fig. S2), the protein levels of TNF-α were significantly decreased, as determined by western blot (Fig. 7f) and ELISA (Fig. 7h). These experimental results indicated that both AuNDs and AuNDs-sCT can effectively reprogram macrophages from an M1 to an M2 phenotype, leveraging their anti-inflammatory effects. This reprogramming is another critical aspect of our "one arrow two eagles" therapeutic strategy in the treatment of inflammatory osteolysis.

Expanding on our significant findings, we next further elucidated the mechanisms underlying the reprogramming of macrophages by AuNDs or AuNDs-sCT. Previous studies have highlighted the nuclear factor kappa B (NF-κB) signaling pathway as a pivotal mediator of macrophage activation [36], oxidative stress injury, and inflammatory-induced osteolysis [37,38]. Hence, we speculated that the inhibition of the NF-κB pathway may participate in the anti-inflammatory effects observed in AuNDs- or AuNDs-sCT-mediated macrophage reprogramming. The NF-κB family, consisting of p50, p52, p65 (Rel-A), c-Rel, and Rel-B, forms homodimers or heterodimers that interact with IκB in the cytoplasm, thereby keeping NF-κB pathway in an inactive state [39]. The heterodimer of p50 and p65, a predominant form activated by the canonical pathway, dissociates from IκB and translocates to the nucleus upon stimulation, where it binds to the promoters of target genes [40,41]. As shown in Fig. 7i, LPS stimulation led to the phosphorylation of NF-κB p65, indicating the activation of NF-κB signaling. However, treatment with AuNDs or AuNDs-sCT significantly suppressed the phosphorylation of NF-κB p65. Besides, immunofluorescence staining revealed that while LPS induced the nuclear translocation of p65, treatment with AuNDs-sCT reduced this effect (Fig. 7j and Fig. S3). These data suggested that AuNDs-sCT, with L-GSH as the ligand, potentially acts as a regulatory "switch" for macrophage polarization, shifting from an M1 to an M2 phenotype. This reprogramming from a pro-inflammatory to an anti-inflammatory state is facilitated by the inhibition of NF-κB p65 phosphorylation, nuclear translocation, and subsequent transcriptional activation changes.

3.6. *In vivo* suppression of calvarial inflammatory osteolysis

Having demonstrated promising anti-inflammatory and anti-resorptive effects *in vitro*, we proceeded to investigate the potential protective and therapeutic effects of AuNDs-sCT on LPS-induced calvarial inflammatory osteolysis *in vivo*. The experimental schedule is outlined in Fig. S4. Specifically, mice were subjected to alternate-day treatments for a total of 4 cycles with either PBS, LPS, or LPS + AuNDs-sCT. On day 7, the mice were euthanized, and the calvarias as along with vital organs (heart, liver, spleen, lung, and kidney) were harvested for subsequent analysis. As shown in Fig. S5, there were no treatment-related mortalities, and body weight between the LPS group and the LPS + AuNDs-sCT group were comparable. Besides, histopathological examination of the collected organs revealed no substantial abnormalities, further confirming the excellent biocompatibility of AuNDs-sCT *in vivo* (Fig. S6).

To evaluate the impacts on bone homeostasis and bone microenvironment in various experimental groups, radiographic and histological assessments were performed. Micro-CT analysis revealed extensive bone erosion on the surface of the calvarial bone, especially at the sagittal suture, in the LPS group. In contrast, treatment with AuNDs-sCT markedly protected against LPS-induced bone loss, as evidenced by a reduction in the area of bone erosion (Fig. 8a). Quantitative analysis further demonstrated a significant increase in key bone mass parameters, such as bone volume/tissue volume (BV/TV), in the AuNDs-sCT group compared to the LPS group (Fig. 8b). These findings provided additional evidence that AuNDs-sCT effectively mitigates LPS-induced inflammatory osteolysis. Consistent with the micro-CT results, hematoxylin-eosin (HE) staining revealed the presence of inflammation and numerous osteoclastic resorption pits in the calvarial bone of the LPS group. However, treatment with AuNDs-sCT significantly alleviated the local extensive osteolysis by reducing both inflammation and the number of osteoclastic resorption pits (Fig. 8c). Furthermore, TRAP staining confirmed a pronounced reduction in the number of OCs (Fig. 8d and f), OC surfaces (Fig. 8e), and eroded surfaces (Fig. 8g) in the AuNDs-sCT group compared to the LPS group. The results were in line with the effects on bone resorption observed with other effective compounds reported in the literature [1,42,43]. Collectively, these findings strongly support the conclusion that AuNDs-sCT effectively prevented LPS-induced inflammatory osteolysis by inhibiting OC differentiation and bone resorptive activity.

To substantiate the *in vivo* anti-inflammatory effect of AuNDs-sCT, we performed immunofluorescence staining of iNOS on mice calvarial sections. Consistent with our *in vitro* findings, LPS stimulation led to a robust expression of iNOS within the bone microenvironment. Nonetheless, treatment with AuNDs-sCT resulted in a significantly reduced iNOS expression levels *in vivo* (Fig. 8h). Meanwhile, treatment with AuNDs-sCT resulted in an increased expression of CD163 *in vivo* (Fig. 8i), which is a well-established marker of M2 macrophages. In summary, AuNDs-sCT possess a dual-mode of action by inhibiting bone resorption and curtailing inflammation. It achieves this by suppressing osteoclastogenesis and the bone resorptive function, as well as by dampening the secretion of inflammatory factors and reprogramming macrophages. Consequently, AuNDs-sCT effectively rescued and protected against LPS-induced inflammatory bone loss.

4. Conclusions

In this study, we successfully developed a multifunctional nanosystem AuNDs-sCT, which effectively reprogrammed macrophages and inhibited osteoclastogenesis to combat inflammatory osteolysis. This innovative approach bridges the gap between innate immunity and bone remodeling, providing a novel perspective of osteoimmunology for the treatment of inflammatory osteolysis. On the one hand, AuNDs-sCT exerted a restraining effect on RANKL-induced OC differentiation by targeting the CTRs on OCs and OC precursors, leading to the downregulation of OC-specific genes and proteins. The specific binding of sCT to CTRs facilitated the anchoring of AuNDs-sCT, resulting in potent anti-resorptive effects at the sites of inflammatory osteolysis. On the other hand, AuNDs-sCT modulated the polarization state of macrophages, shifting from a pro-inflammatory M1 phenotype to an anti-inflammatory M2 phenotype, an effect mediated by inhibiting the phosphorylation of

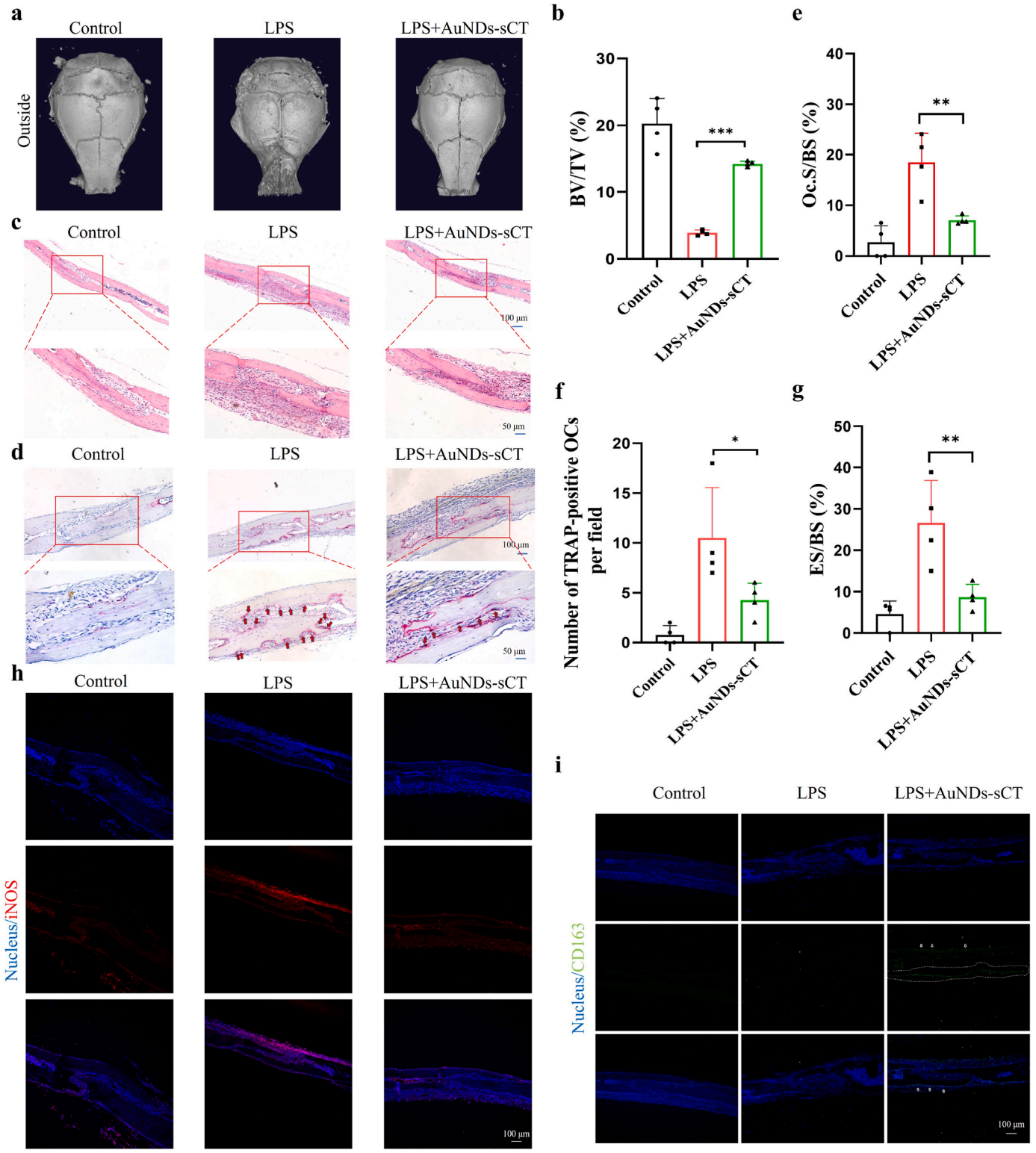

Fig. 8. ***In vivo*** **suppression of calvarial inflammatory osteolysis by AuNDs-sCT.** (a) Representative images of calvaria reconstructed by a micro-CT scanner. (b) Quantification of BV/TV in the sagittal suture of the calvaria (n = 4). (c) Representative images of HE staining on histological sections of mouse calvaria (scale bars: top, 100 μm; bottom, 50 μm). (d) Representative images of TRAP staining on histological sections of mouse calvaria (scale bars: top, 100 μm; bottom, 50 μm). (e) Ratio of TRAP-positive cells/bone surface. (f) Number of TRAP-positive OCs per field. (g) Eroded surface per bone surface. Immunofluorescent staining of (h) iNOS (red) and CD163 (green) in calvarial sections using CLSM (scale bars: 100 μm). $^{*}P < 0.05$, $^{**}P < 0.01$, $^{***}P < 0.001$. (For interpretation of the references to colour in this figure legend, the reader is referred to the Web version of this article.)

NF-κB p65. The targeting effect of sCT further enhanced the durability and efficacy of AuNDs-sCT as an anti-inflammatory agent at the sites of inflammatory osteolysis. By reprogramming macrophages and inhibiting osteoclastogenesis, AuNDs-sCT achieved a "one arrow two eagles" therapeutic strategy. Overall, the designed AuNDs-sCT, realizing drug repurposing, holds great promise as a therapeutic approach for the clinical management of inflammatory osteolysis. Additionally, promising fluorescent properties of AuNDs-sCT enabled the real-time visualization of therapeutic process, facilitating precise control over drug administration.

CRediT authorship contribution statement

Tong Sha: Writing – original draft, Visualization, Validation, Software, Methodology, Investigation, Formal analysis, Data curation, Conceptualization. **Ze Wang:** Writing – original draft, Visualization, Validation, Software, Methodology, Investigation, Formal analysis, Data curation, Conceptualization. **Jinwei Li:** Software, Methodology, Investigation, Data curation. **Yahong Wu:** Software, Methodology, Investigation. **Jinbiao Qiang:** Software, Methodology, Investigation. **Zhenming Yang:** Software, Methodology, Investigation. **Yue Hu:** Methodology, Funding acquisition. **Kaijuan Zheng:** Software, Methodology. **Shuyu Zhang:** Software, Methodology. **Haizhu Sun:** Supervision. **Andrew K. Whittaker:** Supervision. **Bai Yang:** Supervision. **Hongchen Sun:** Supervision, Funding acquisition. **Quan Lin:** Writing – review & editing, Visualization, Validation, Supervision, Funding acquisition, Formal analysis, Data curation, Conceptualization. **Ce Shi:** Writing – review & editing, Visualization, Validation, Supervision, Investigation, Funding acquisition, Formal analysis, Data curation, Conceptualization.

Declaration of competing interest

The authors declare that they have no known competing financial interests or personal relationships that could have appeared to influence the work reported in this paper.

Data availability

Data will be made available on request.

Acknowledgements

This work was supported by the National Natural Science Foundation of China (Nos. 82270959 and 81970903), the National Key Research and Development Program of China (2022YFC2504200), the Natural Science Foundation of Jilin Province (No. SKL202302002), the Key Research and Development Project of Jilin Provincial Science and Technology Department (No. 20210204142YY), the Jilin University Norman Bethune Program (No. 2023B28), the Fundamental Research Funds for the Central Universities, the Natural Science Foundation of Liaoning Province (No. 2022BS-123), the Science and Technology Project of Shenyang (No. 21-173-9-34), "Medical + X" Interdisciplinary Innovation Team "Announcement and Leadership" Construction Project (2022JBGS08), and the National Natural Science Foundation of China (Nos. 21574018 and 51433003).

Appendix A. Supplementary data

Supplementary data to this article can be found online at https://doi.org/10.1016/j.mtbio.2024.101285.

References

[1] L. Wei, W. Chen, L. Huang, H. Wang, Y. Su, J. Liang, H. Lian, J. Xu, J. Zhao, Q. Liu, Alpinetin ameliorates bone loss in LPS-induced inflammation osteolysis via ROS mediated P38/PI3K signaling pathway, Pharmacol. Res. 184 (2022) 106400.
[2] M. Eger, S. Hiram-Bab, T. Liron, N. Sterer, Y. Carmi, D. Kohavi, Y. Gabet, Mechanism and prevention of titanium particle-induced inflammation and osteolysis, Front. Immunol. 9 (2018) 2963.
[3] W. Deng, Z. Ding, Y. Wang, B. Zou, J. Zheng, Y. Tan, Q. Yang, M. Ke, Y. Chen, S. Wang, X. Li, Dendrobine attenuates osteoclast differentiation through modulating ROS/NFATc1/MMP9 pathway and prevents inflammatory bone destruction, Phytomedicine 96 (2022) 153838.
[4] S.B. Cohen, R.K. Dore, N.E. Lane, P.A. Ory, C.G. Peterfy, J.T. Sharp, D. van der Heijde, L. Zhou, W. Tsuji, R. Newmark, Denosumab treatment effects on structural damage, bone mineral density, and bone turnover in rheumatoid arthritis: a twelve-month, multicenter, randomized, double-blind, placebo-controlled, phase II clinical trial, Arthritis Rheum. 58 (5) (2008) 1299–1309.
[5] G. Mbalaviele, D.V. Novack, G. Schett, S.L. Teitelbaum, Inflammatory osteolysis: a conspiracy against bone, J. Clin. Invest. 127 (6) (2017) 2030–2039.
[6] H. Takayanagi, Osteoimmunology: shared mechanisms and crosstalk between the immune and bone systems, Nat. Rev. Immunol. 7 (4) (2007) 292–304.
[7] C. Feng, L. Pan, X. Qin, D. Li, T. Chen, Z. Lin, G. Li, Q. Wang, Inflammation-homing "living drug depot" for efficient arthritis treatment, Acta Biomater. 150 (2022) 324–336.
[8] H. Huang, S. Zheng, J. Wu, X. Liang, S. Li, P. Mao, Z. He, Y. Chen, L. Sun, X. Zhao, A. Cai, L. Wang, H. Sheng, Q. Yao, R. Chen, Y.-Z. Zhao, L. Kou, Opsonization inveigles macrophages engulfing carrier-free bilirubin/jph203 nanoparticles to suppress inflammation for osteoarthritis therapy, Adv. Sci. 11 (22) (2024) e2400713.
[9] C. Varol, A. Mildner, S. Jung, Macrophages: development and tissue specialization, Annu. Rev. Immunol. 33 (2015) 643–675.
[10] S. Wang, M. Lu, W. Wang, S. Yu, R. Yu, C. Cai, Y. Li, Z. Shi, J. Zou, M. He, W. Xie, D. Yu, H. Jin, H. Li, W. Xiao, C. Fan, F. Wu, Y. Li, S. Liu, Macrophage polarization modulated by NF-κB in polylactide membranes-treated peritendinous adhesion, Small 18 (13) (2022) e2104112.
[11] C. Ding, C. Yang, T. Cheng, X. Wang, Q. Wang, R. He, S. Sang, K. Zhu, D. Xu, J. Wang, X. Liu, X. Zhang, Macrophage-biomimetic porous Se@SiO2 nanocomposites for dual modal immunotherapy against inflammatory osteolysis, J. Nanobiotechnol. 19 (1) (2021) 382.
[12] D. Yang, Y. Wan, Molecular determinants for the polarization of macrophage and osteoclast, Semin. Immunopathol. 41 (5) (2019) 551–563.
[13] A. Shapouri-Moghaddam, S. Mohammadian, H. Vazini, M. Taghadosi, S.-A. Esmaeili, F. Mardani, B. Seifi, A. Mohammadi, J.T. Afshari, A. Sahebkar, Macrophage plasticity, polarization, and function in health and disease, J. Cell. Physiol. 233 (9) (2018) 6425–6440.
[14] Y. Liu, P. Yu, X. Peng, Q. Huang, M. Ding, Y. Chen, R. Jin, J. Xie, C. Zhao, J. Li, Hexapeptide-conjugated calcitonin for targeted therapy of osteoporosis, J. Contr. Release 304 (2019) 39–50.
[15] M. Ikegame, S. Ejiri, H. Ozawa, Calcitonin-induced change in serum calcium levels and its relationship to osteoclast morphology and number of calcitonin receptors, Bone 35 (1) (2004) 27–33.
[16] S. Cao, Y. Liu, H. Shang, S. Li, J. Jiang, X. Zhu, P. Zhang, X. Wang, J. Li, Supramolecular nanoparticles of calcitonin and dipeptide for long-term controlled release, J. Contr. Release 256 (2017) 182–192.
[17] L. Bandeira, E.M. Lewiecki, J.P. Bilezikian, Pharmacodynamics and pharmacokinetics of oral salmon calcitonin in the treatment of osteoporosis, Expet Opin. Drug Metabol. Toxicol. 12 (6) (2016) 681–689.
[18] S. Pushpakom, F. Iorio, P.A. Eyers, K.J. Escott, S. Hopper, A. Wells, A. Doig, T. Guilliams, J. Latimer, C. McNamee, A. Norris, P. Sanseau, D. Cavalla, M. Pirmohamed, Drug repurposing: progress, challenges and recommendations, Nat. Rev. Drug Discov. 18 (1) (2019) 41–58.
[19] H. Zhou, H. Liu, Y. Yu, X. Yuan, L. Xiao, Informatics on drug repurposing for breast cancer, Drug Des. Dev. Ther. 17 (2023) 1933–1943.
[20] Z. Wang, X. Ren, D. Wang, L. Guan, X. Li, Y. Zhao, A. Liu, L. He, T. Wang, A. V. Zvyagin, B. Yang, Q. Lin, Novel strategies for tumor radiosensitization mediated by multifunctional gold-based nanomaterials, Biomater. Sci. 11 (4) (2023) 1116–1136.
[21] S.-M. Lee, H.J. Kim, Y.-J. Ha, Y.N. Park, S.-K. Lee, Y.-B. Park, K.-H. Yoo, Targeted chemo-photothermal treatments of rheumatoid arthritis using gold half-shell multifunctional nanoparticles, ACS Nano 7 (1) (2013) 50–57.
[22] Y.Y. Su, X.Y. Jiang, L.J. Zheng, Y.W. Yang, S.Y. Yan, Y. Tian, W. Tian, W.F. Liu, Z. G. Teng, H. Yao, S.J. Wang, L.J. Zhang, Hybrid Au-star@Prussian blue for high-performance towards bimodal imaging and photothermal treatment, J Colloid Interf Sci 634 (2023) 601–609.
[23] X. Wang, M. Jiao, F. Tian, X. Lu, H. Xiong, F. Liu, Y. Wan, X. Zhang, H. Wan, A biomimetic nanoplatform with improved inflammatory targeting behavior for ROS scavenging-based treatment of ulcerative colitis, Adv Healthc Mater 12 (29) (2023) e2301450.
[24] F. Gao, Q. Yuan, P. Cai, L. Gao, L. Zhao, M. Liu, Y. Yao, Z. Chai, X. Gao, Au clusters treat rheumatoid arthritis with uniquely reversing cartilage/bone destruction, Adv. Sci. 6 (7) (2019) 1801671.
[25] H. Chen, Y. Jiang, T. Xu, J. Xu, J. Yu, Z. Chu, Y. Jiang, Y. Song, H. Wang, H. Qian, Au nanocluster-modulated macrophage polarization and synoviocyte apoptosis for enhanced rheumatoid arthritis treatment, J. Mater. Chem. B 10 (25) (2022) 4789–4799.

[26] M.L. Guo, G. Zhang, R.L. Zhao, H.Z. Ma, Y.X. Yan, S.Y. Yang, J. Meng, Y. Huang, X. D. Zhang, H. Wang, R.P. Zhang, Ligand engineering of gold nanoclusters for NIR-II imaging, ACS Appl. Nano Mater. 6 (17) (2023) 15945–15958.
[27] Y.Q. Sun, D.D. Wang, Y.Q. Zhao, T.X. Zhao, H.C. Sun, X.W. Li, C.X. Wang, B. Yang, Q. Lin, Polycation-functionalized gold nanodots with tunable near-infrared fluorescence for simultaneous gene delivery and cell imaging, Nano Res. 11 (5) (2018) 2392–2404.
[28] Z. Wang, A. Liu, X. Li, L. Guan, H. Xing, L. He, L. Fang, A.V. Zvyagin, X. Yang, B. Yang, Q. Lin, Multifunctional nanoprobe for multi-mode imaging and diagnosis of metastatic prostate cancer, Talanta 256 (2023) 124255.
[29] Z. Wang, L. He, S. Che, H. Xing, L. Guan, Z. Yang, X. Li, A.V. Zvyagin, Q. Lin, W. Qu, AuNCs-LHRHa nano-system for FL/CT dual-mode imaging and photothermal therapy of targeted prostate cancer, J. Mater. Chem. B 10 (27) (2022) 5182–5190.
[30] Y.X. Liu, M.D. Cao, Z.X. Huang, C.M. Yu, N.D. Yang, Q. Wu, L. Shi, W.J. Duan, Y. Zhu, J.F. Wei, L. Li, W. Huang, Ultrasensitive detection of IgE levels based on magnetic nanocapturer linked immunosensor assay for early diagnosis of cancer, Chinese Chem Lett 33 (4) (2022) 1855–1860.
[31] T. Maleitzke, A. Hildebrandt, T. Dietrich, J. Appelt, D. Jahn, E. Otto, D. Zocholl, A. Baranowsky, G.N. Duda, S. Tsitsilonis, J. Keller, The calcitonin receptor protects against bone loss and excessive inflammation in collagen antibody-induced arthritis, iScience 25 (1) (2022) 103689.
[32] F. Song, C. Wei, L. Zhou, A. Qin, M. Yang, J. Tickner, Y. Huang, J. Zhao, J. Xu, Luteoloside prevents lipopolysaccharide-induced osteolysis and suppresses RANKL-induced osteoclastogenesis through attenuating RANKL signaling cascades, J. Cell. Physiol. 233 (2) (2018) 1723–1735.
[33] F. Fu, S. Shao, Z. Wang, F. Song, X. Lin, J. Ding, C. Li, Z. Wu, K. Li, Y. Xiao, Y. Su, J. Zhao, Q. Liu, J. Xu, Scutellarein inhibits RANKL-induced osteoclast formation in vitro and prevents LPS-induced bone loss in vivo, J. Cell. Physiol. 234 (7) (2019) 11951–11959.
[34] F. Xing, L. Geng, H. Guan, D. Liu, Y. Li, L. Zeng, Y. Chen, R. Tian, Z. Li, R. Cao, Y. Zhao, P. Yan, H. Qiang, N. Kong, K. Wang, P. Yang, Astragalin mitigates inflammatory osteolysis by negatively modulating osteoclastogenesis via ROS and MAPK signaling pathway, Int. Immunopharm. 112 (2022) 109278.
[35] Y. Xie, L. Jiang, J. Qiu, Y. Wang, A comparative evaluation of the immunotoxicity and immunomodulatory effects on macrophages exposed to aromatic trihalogenated DBPs, Immunopharmacol. Immunotoxicol. 41 (2) (2019) 319–326.
[36] C.-F. Chang, K.-C. Liao, C.-H. Chen, 2-Phenylnaphthalene derivatives inhibit lipopolysaccharide-induced pro-inflammatory mediators by downregulating of MAPK/NF-κB pathways in RAW 264.7 macrophage cells, PLoS One 12 (1) (2017) e0168945.
[37] H. Li, Z. Zhai, G. Liu, T. Tang, Z. Lin, M. Zheng, A. Qin, K. Dai, Sanguinarine inhibits osteoclast formation and bone resorption via suppressing RANKL-induced activation of NF-κB and ERK signaling pathways, Biochem. Biophys. Res. Commun. 430 (3) (2013) 951–956.
[38] Z. Wang, D.Z. Wang, X.J. Ren, Z.S. Liu, A.N. Liu, X.C. Li, L. Guan, Y.N. Shen, S. Z. Jin, A.V. Zvyagin, B. Yang, T.J. Wang, Q. Lin, One stone, three birds: multifunctional nanodots as "pilot light" for guiding surgery, enhanced radiotherapy, and brachytherapy of tumors, Acs Central Sci 9 (10) (2023) 1976–1988.
[39] S. Giridharan, M. Srinivasan, Mechanisms of NF-κB p65 and strategies for therapeutic manipulation, J. Inflamm. Res. 11 (2018) 407–419.
[40] A. Oeckinghaus, S. Ghosh, The NF-kappaB family of transcription factors and its regulation, Cold Spring Harb Perspect Biol 1 (4) (2009) a000034.
[41] C.-P. Liu, X. Zhang, Q.-L. Tan, W.-X. Xu, C.-Y. Zhou, M. Luo, X. Li, R.-Y. Huang, X. Zeng, NF-κB pathways are involved in M1 polarization of RAW 264.7 macrophage by polyporus polysaccharide in the tumor microenvironment, PLoS One 12 (11) (2017) e0188317.
[42] Z. Wu, H. Wu, C. Li, F. Fu, J. Ding, S. Shao, K. Li, X. Yu, Y. Su, J. Liang, X. Lin, G. Yuan, J. Zhou, F. Song, J. Zhao, J. Xu, Q. Liu, F. Xu, Daphnetin attenuates LPS-induced osteolysis and RANKL mediated osteoclastogenesis through suppression of ERK and NFATc1 pathways, J. Cell. Physiol. 234 (10) (2019) 17812–17823.
[43] K. Gan, H. Lian, T. Yang, J. Huang, J. Chen, Y. Su, J. Zhao, J. Xu, Q. Liu, Periplogenin attenuates LPS-mediated inflammatory osteolysis through the suppression of osteoclastogenesis via reducing the NF-κB and MAPK signaling pathways, Cell Death Discov 10 (1) (2024) 86.